Available online at www.sciencedirect.com
ScienceDirect
Journal of Magnesium and Alloys xxx (xxxx) xxx
www.elsevier.com/locate/jma

Full Length Article

Corrosion resistance of Mg-Al-LDH steam coating on AZ80 Mg alloy: Effects of citric acid pretreatment and intermetallic compounds

Jin-Meng Wang[a], Xiang Sun[a], Liang Song[a], M. Bobby Kannan[b,c], Fen Zhang[a,*], Lan-Yue Cui[a], Yu-Hong Zou[d], Shuo-Qi Li[a], Rong-Chang Zeng[a,e,*]

[a] *Corrosion Laboratory for Light Metals, College of Materials Science and Engineering, Shandong University of Science and Technology, Qingdao 266590, China*
[b] *School of Engineering, University of Newcastle, Callaghan, New South Wales 2308, Australia*
[c] *College of Science and Engineering, James Cook University, Townsville, Queensland 4811, Australia*
[d] *College of Chemical and Environmental Engineering, Shandong University of Science and Technology, Qingdao 266590, China*
[e] *School of Materials Science and Engineering, Zhengzhou University, Zhengzhou 450002, China*

Received 2 September 2021; received in revised form 26 November 2021; accepted 3 January 2022
Available online xxx

Abstract

In this study, the effects of intermetallic compounds ($Mg_{17}Al_{12}$ and Al_8Mn_5) on the Mg-Al layered double hydroxide (LDH) formation mechanism and corrosion behavior of an in-situ LDH/$Mg(OH)_2$ steam coatings on AZ80 Mg alloy were investigated. Citric acid (CA) was used to activate the alloy surface during the pretreatment process. The alloy was first pretreated with CA and then subjected to a hydrothermal process using ultrapure water to produce Mg-Al-LDH/$Mg(OH)_2$ steam coating. The effect of different time of acid pretreatment on the activation of the intermetallic compounds was investigated. The microstructure and elemental composition of the obtained coatings were analyzed using FE-SEM, EDS, XRD and FT-IR. The corrosion resistance of the coated samples was evaluated using different techniques, i.e., potentiodynamic polarization (PDP), electrochemical impedance spectrum (EIS) and hydrogen evolution test. The results indicated that the CA pretreatment significantly influenced the activity of the alloy surface by exposing the intermetallic compounds. The surface area fraction of $Mg_{17}Al_{12}$ and Al_8Mn_5 phases on the surface of the alloy was significantly higher after the CA pretreatment, and thus promoted the growth of the subsequent Mg-Al-LDH coatings. The CA pretreatment for 30 s resulted in a denser and thicker LDH coating. Increase in the CA pretreatment time significantly led to the improvement in corrosion resistance of the coated AZ80 alloy. The corrosion current density of the coated alloy was lower by three orders of magnitude as compared to the uncoated alloy.

Keywords: Magnesium alloy; Citric acid pretreatment; Steam coating; Layered double hydroxide; Intermetallic compounds; Corrosion resistance.

1. Introduction

Magnesium (Mg) and its alloys have attractive physical and mechanical properties such as high specific strength and stiffness, electromagnetic shielding and high damping capacity [1–4]. Hence, they are excellent candidate materials for automotive and aeronautical applications where weight reduction is critical for fuel saving purpose. However, their poor corrosion resistance limits their widespread in industrial applications [5–12].

In order to improve the corrosion resistance of Mg, two methods are generally used: (i) alloying, and (ii) surface modification [13,14]. Surface modification process is widely studied to increase the corrosion resistance of magnesium and its alloys [15]. The surface modification techniques include micro-arc oxidation [16–18], chemical conversion coating [19–21], layer-by-layer assembly [22–24] and electroless plating [25–27].

Recently, layered double hydroxide (LDH) coating has been developed as a new smart coating, which can be used

* Corresponding authors.
E-mail addresses: zhangfen2011@hotmail.com (F. Zhang), rczeng@foxmail.com (R.-C. Zeng).

https://doi.org/10.1016/j.jma.2022.01.004

Please cite this article as: J.-M. Wang, X. Sun, L. Song et al., Corrosion resistance of Mg-Al-LDH steam coating on AZ80 Mg alloy: Effects of citric acid pretreatment and intermetallic compounds, Journal of Magnesium and Alloys, https://doi.org/10.1016/j.jma.2022.01.004

as a nanocontainer by adjusting the types of anions between the layers [28–37]. LDH is present in natural minerals, but can also be synthesized [38–40]. The chemical formula of LDH is $[M^{2+}_{1-x}M^{3+}_{x}(OH)_2]_x(A^{n-})_{x/n}\bullet mH_2O$. The layers of LDH are composed of divalent and trivalent metal ions and hydroxides arranged in octahedrons, and the main layers are all composed of anions [39,41]. The properties of LDH are mainly influenced by the types of metallic ions and interlayer anions, ion radius and charge number, which can affect the composition of the main LDH laminate, the number and types of interlayer anions. The size of LDH can be adjusted and it possesses diversified functions, such as flame retardant performance, ion exchange performance, thermal stability performance, infrared absorption performance, catalytic performance and corrosion resistance [31,42,43]. Until now, the main preparation methods of LDH have been hydrothermal treatment and co-precipitation method. The disadvantages of these preparation methods of LDH coating include long reaction time, use of toxic chemicals, and complex operation. Hence, it is necessary to develop an environmentally friendly and relatively simple method. *In-situ* steam coating method has attracted wide attention in recent years for its effective coating ability on materials. It is a chemical-free method and uses ultrapure water as the steam source for the coating [44–46]. It is an excellent method for protection of Mg and its alloys due to its non-toxic and environmentally friendly characteristics [28,44].

The aluminium (Al) content on the surface of the Mg alloy is critical to the preparation of the LDH coating by the in-situ steam method. While the Al content of the untreated magnesium alloy matrix is far from reaching the requirement. Acid pretreatment is an effective method to activate the second phase, which contains the Al species. In the acid pretreatment process, the α-Mg phase as the anode corrodes, and the second phase as the cathode is basically unaffected, therefore increases the exposure of the second phase particles (Al-containing species) on the alloy surface, leading to an increasement of the Al content on the surface of the Mg alloy [7,47,48]. The larger amount of Al provided by the above acid pretreatment is beneficial to the subsequent growth of the coating.

Corrosion pits are easy to appear on the surface of the Mg alloy when pretreated with strong acid. Strong acid treatment will cause excessive corrosion, leaving behind many corrosion pits due to the falling of the second phase particles. The localized pitting corrosion is harmful to the substrate [49,50]. Citric acid (CA) taken from fruits and vegetables as an organic acid, is an edible acid, which is widely distributed in nature [51]. Therefore, it is a good choice to choose CA for pretreating the substrate. It is expected that acid pretreatment is a simple and effective method to expose the second phase on the surface of the Mg alloy, which may promote the growth of the subsequent LDH coatings.

This study aims to investigate the effect of CA pretreatment time on the revealing of surface intermetallic compounds ($Mg_{17}Al_{12}$ and Al_8Mn_5), and the formation and corrosion resistance of Mg-Al-LDH coating on AZ80 Mg alloy. Firstly, the alloy was pretreated with CA with different times, and then the steam coating was prepared on the alloy by the in-situ steam method. When the Mg-Al-LDH coating is prepared by the steam method, the source of both Mg^{2+} and Al^{3+} ions, required in the growth process of the LDH coating, comes from the Mg-Al alloy substrate. The substrate can provide sufficient Mg^{2+} ions for the reaction. However, the amount of Al^{3+} ions that can participate in the reaction on the surface of the substrate are by far insufficient, which limits the growth of subsequent LDH coatings. Therefore, it is necessary to perform acid pretreatment to increase the exposure of the second phase particles (which contain Al) on the alloy surface.

2. Experimental

2.1. Materials and chemicals

As-extruded AZ80 magnesium alloy (supplied by Dongguan Kangji Magnesium Industry Co., Ltd.) with dimensions of 20 × 20 × 5 mm was used as the substrate in this study. Prior to the experiment, the samples were polished to 2500# with SiC sandpaper, and then rinsed with deionized water and dried in air.

2.2. Preparation of the coatings

Fig. 1 shows the experimental preparation process of the LDH coating prepared by the steam method. The AZ80 magnesium alloy was immersed in 20 g/L CA solution for 10 s, 20 s, 30 s and 45 s, and then washed with deionized water and absolute ethanol. 20 mL of pure water was added into a 100 mL Teflon-lined autoclave, in which the polished AZ80 magnesium alloy sample was suspended with a cotton thread such that the alloy was 2-3 cm above the liquid surface. The autoclave was then transferred to an oven and heated to 433 K for 6 h to obtain the LDH coatings. Based on the pretreatment time, the samples were designated as CA/AZ80–10s, CA/AZ80–20s, CA/AZ80–30s and CA/AZ80–45s, and after the in-situ steam reaction, the coated samples were designated as CA/LDH-10s, CA/LDH-20s, CA/LDH-30s and CA/LDH-45s.

2.3. Characterization of the coatings

2.3.1. Surface morphology and composition analysis

The surface morphologies of the coatings were observed using field-emission scanning electron microscopy (SEM, Nova Nano SEM 450, USA). The surface roughness was measured using a Zeta-20 3D-morphologies optical profilometer. An average roughness Ra was obtained based on over 5 values measured at different positions. The elemental compositions of the coatings were analyzed using X-ray energy spectrometer (EDS). The phase composition of the samples was detected by X-ray diffractometer (XRD, Rigaku Utima IV, Japan) with the scanning angle of 5–80° and scanning speed of 8 °min^{-1}.

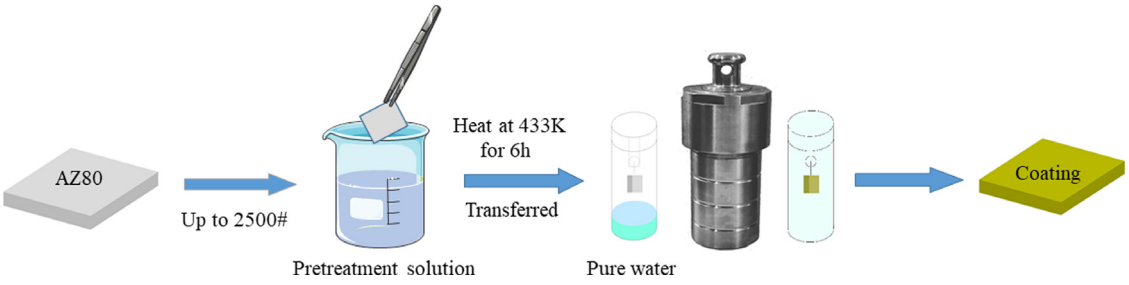

Fig. 1. Schematic diagram of preparation process of LDH coatings after acid pretreatment of AZ80 Mg alloy.

The functional groups and the chemical bonds in the coating were detected by a Fourier Infrared Spectrometer (FT-IR, Thermo Fisher Scientific, Nicolet 380, USA) and X-ray photoelectron spectroscopy (XPS, ESCALAB XI+, Thermo Fisher Scientific, USA) with an energy resolution of 100 eV wide spectrum and 20 eV narrow spectrum.

2.3.2. Corrosion resistance measurements

The microstructure of the alloy was examined using an optical microscope (OM, Olympus-GX41, Japan). The corrosion properties were evaluated using an electrochemical Princeton potentiostat (PARSTAT2273, Princeton Instruments Corporation, USA) apparatus and a classical three-electrode cell, consisting of the specimen with an exposed area of 1 cm^2 as the working electrode, saturated calomel as the reference electrode and a platinum mesh as the counter electrode. All the experiments were conducted in 3.5 wt.% NaCl solution at room temperature. Electrochemical impedance spectroscopy (EIS) measurements on the samples were carried out at their open-circuit potential (OCP) with a peak-to-peak amplitude of 10 mV in the frequency range from 100 kHz to 10 mHz. Equivalent circuit model was used to fit the EIS curves with the help of ZSimpWin software. Potentiodynamic polarization (PDP) test was performed by scanning the potential of the sample from −2.0 to −0.3 V at a scan rate of 2.0 mV s^{-1}.

In addition, hydrogen evolution tests were carried out to characterize the corrosion behavior of the coated samples. The hydrogen evolution was tested by placing the samples with the full surface area exposed to 3.5 wt.% NaCl solution at 25.0 ± 0.1 °C under an inverted funnel connected to a graduated burette and measuring the change in the solution level in the burette intermittently for 228 h [19,52–54].

3. Result and discussion

3.1. Surface characterizations

Fig. 2 shows the optical microstructure of the polished alloy and CA pretreated alloy as well as the surface area fraction of the second phase particles. As observed in Fig. 2a, there are a small amount of second phase particles ($Mg_{17}Al_{12}$ and Al_8Mn_5) on the surface of the polished alloy Fig. 2b–d shows that with the increase of CA treatment time, the number of second phase particles on the surface of the alloy

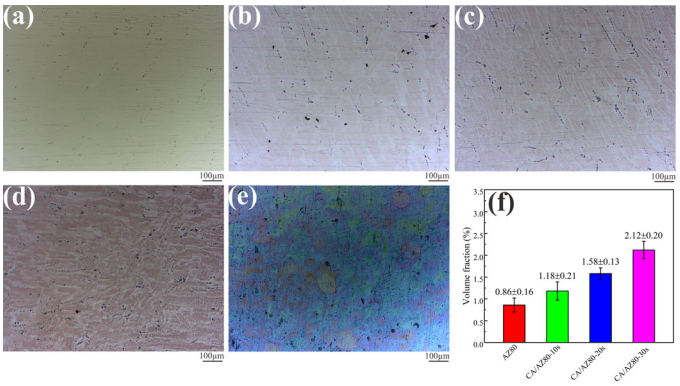

Fig. 2. Optical microstructure of (a) polished AZ80, (b) CA/AZ80–10s, (c) CA/AZ80−20s, (d) CA/AZ80–30s and (e) CA/AZ80–45s and (f) the second phase surface area fraction of polished AZ80 CA/AZ80–10s, CA/AZ80–20s and CA/AZ80–30s.

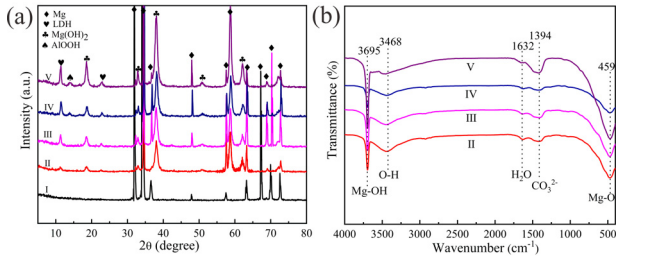

Fig. 3. (a) XRD patterns and (b) FT-IR spectra of (I) Mg alloy AZ80, (II) LDH, (III) CA/LDH-10s, (IV) CA/LDH-20s (V) CA/LDH-30s.

increases significantly. Interestingly, the surface color of the CA/AZ80–45s sample changed greatly (Fig. 2e), which may be due to high corrosion, and leaving behind many corrosion pits due to the falling of the second phase particles. Hence, corrosion damages are apparent on the surface of the sample.

As seen in Fig. 2f, the surface area fraction of the second phase particles increases as follows: 1.5 times after the pretreatment for 10 s; 2 times after the pretreatment for 20 s; 3 times after the pretreatment for 30 s. This change indicates that acid pretreatment duration influences the exposure of second phase particles on the alloy surface.

Fig. 3a shows the XRD pattern of the alloy and different LDH coatings. It can be seen from Fig. 3a that all the LDH coatings have two peaks at approximately 11.3° and 22.6°, corresponding to the (003) and (006) diffraction peaks, respectively, of the LDH. This indicates that the LDH coat-

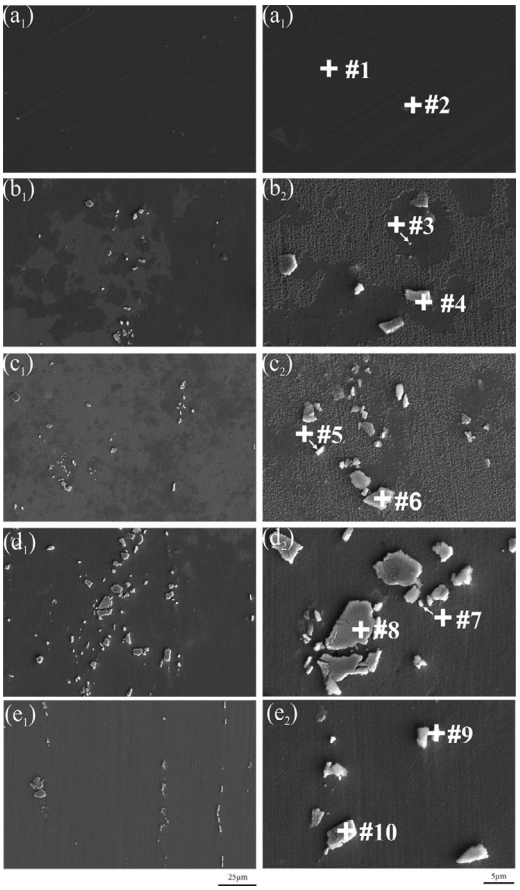

Fig. 4. SEM images of (a) polished AZ80, (b) CA/AZ80−10s, (c) CA/AZ80–20s (d) CA/AZ80−30s and (e) CA/AZ80–45s.

ing was successfully formed on the alloy. At the same time, Fig. 3 also shows the characteristic peaks of $Mg(OH)_2$ at 18.4°, 37.9° and 58.6°. Hence, it is confirmed that the coating is mainly composed of $Mg(OH)_2$ and Mg-Al-LDH. It is noted that the intensities of (003) and (006) planes of LDH coatings change with different pretreatment time. As compared with the other samples, the CA/LDH-30s samples have the strongest LDH phase diffraction peak, indicating that the LDH content is relatively high.

Fig. 3b shows the FT-IR spectra of the different LDH coatings. The peak at 3695 cm^{-1} corresponds to the Mg-OH stretching vibration, and the absorption peak at 3468 cm^{-1} corresponds to the O-H stretching vibration, which is due to the presence of surface absorption water and interlayer water molecules. In addition, the absorption peak recorded at 1632 cm^{-1} is attributed to the stretching vibration of the hydroxyl group -OH in the water molecule. The absorption peak at 1394 cm^{-1} is caused by the stretching vibration of CO_3^{2-}, whereas the absorption peak at 459 cm^{-1} corresponds to the stretching vibration of the Mg-O bond. The existence of these absorption peaks confirms the formation of Mg-Al-CO_3^{2-}-LDH. Therefore, it can be concluded that the LDH coating can be successfully formed on AZ80 Mg alloy by acid pretreatment and then by in-situ steam method.

Table 1
Elemental compositions of selected spectrum on AZ80 as shown in Fig. 4 (at.%).

Point	Mg	Al	Mn	Mg/Al	Al/Mn	Total
#1	97.79	2.06	0.15	–	–	100
#2	21.97	52.11	25.92	–	–	100
#3	50.89	36.86	–	17/12	–	100
#4	7.29	60.35	32.65	–	9/5	100
#5	51.48	48.52	–	18/12	–	100
#6	6.78	60.21	39.96	–	7.5/5	100
#7	61.49	38.51	–	19/12	–	100
#8	6.05	57.65	36.30	–	8/5	100
#9	57.14	42.86	–	16/12	–	100
#10	10.13	52.42	37.45	–	7/5	100

Fig. 4 shows the SEM micrographs of the polished and coated alloy samples. There is no obvious second phase particles on the surface of the polished alloy (Fig. 4a), which is due to the coverage of the oxide and hydroxide layer on the surface of the alloy Fig. 4b–d suggests that through CA pretreatment, the α-Mg phase dissolves and the second phase particles appear. As compared with the polished alloy, after the CA pretreatment, the second phase particles on the surface of the alloy are clearly evident, and with the increase in the treatment time, the exposure of the second phase particles on the surface of the CA/AZ80–30s sample is the largest. Beside, the number of the second phase particles was reduced, and corrosion pits appeared on the surface of the CA/AZ80–45s sample. The second phase particles containing Al provide a large number of nucleation sites for the growth of the LDH coating and also play an active role in the growth of the coating. Table 1 shows the elemental composition on the surface of the alloy after acid pretreatment (Fig. 4). From the elemental composition (in points 3–10), it can be seen that the second phase particles present on the surface of the alloy include Al_8Mn_5 and $Mg_{17}Al_{12}$ (known as β phase), which is in agreement with the literatures [55,56].

Fig. 5 shows the three-dimensional topography of the samples as well as the corresponding surface roughness data. The surface roughness values can be arranged in ascending order as follows: polished AZ80 (10.21 ± 1.19 nm) < CA/AZ80–10s (17.26 ± 1.47 nm) < CA/AZ80–20s (25.96 ± 3.21 nm) < CA/AZ80–45s (26.52 ± 2.34 nm) < CA/AZ80–30s (33.54 ± 4.45 nm). The surface roughness value of CA/AZ80–30s is the largest, which is mainly due to the increase in the number and size of the second phase particles on the surface of the alloy after acid pretreatment. The surface roughness value of CA/AZ80–45s decreased, which was in accordance with the optical microstructures shown in Fig. 2 and SEM images of second phase particles shown in Fig. 4.

Fig. 6 is SEM micrographs and EDS results of the different LDH coatings. It can be seen from Fig. 6a that the surface of the LDH coating formed without acid pretreatment is relatively loose, and the size of the nanosheets as well as the pores between the nanosheets are relatively large. From Fig. 6b–d, it can be observed that the surface of the LDH

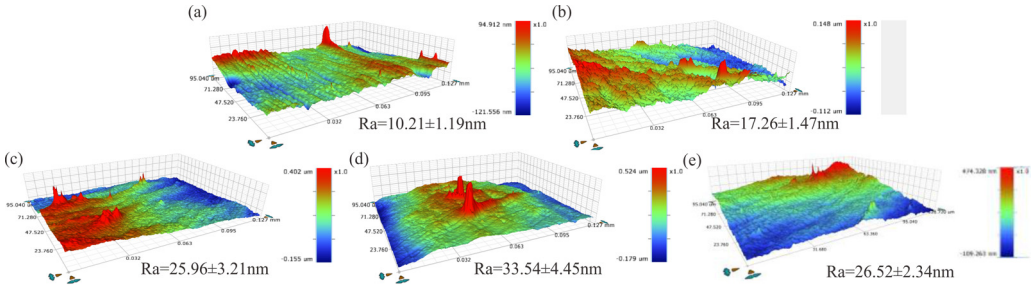

Fig. 5. Surface 3D-morphologies of (a) polished AZ80, (b) CA/AZ80–10s, (c) CA/AZ80–20s and (d) CA/AZ80–30s (e) CA/AZ80–45s and the corresponding roughness.

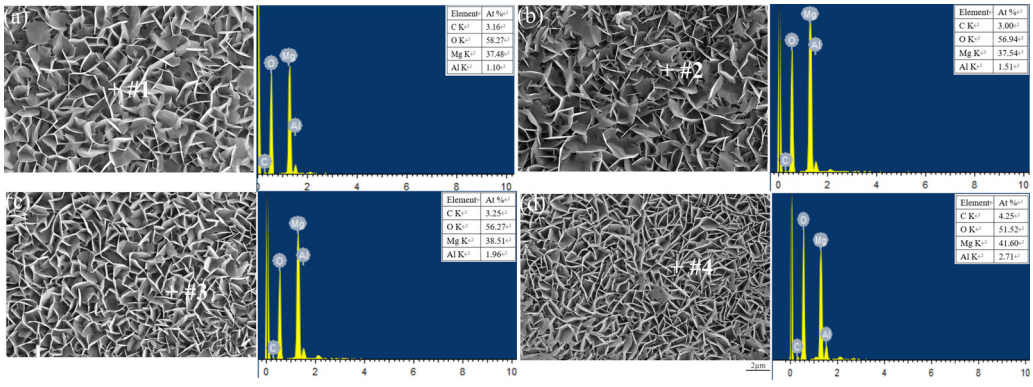

Fig. 6. SEM images and EDS results of (a) LDH, (b) CA/LDH-10s, (c) CA/LDH-20s and (d) CA/LDH-30s.

coating prepared after acid pretreatment is denser than that of the LDH coating without acid pretreatment, and also as the pretreatment time increases, the density of the LDH coating increases significantly. Among all the coatings, the surface morphology of the CA/LDH-30s coating is the densest, and the size of the nanoplates as well as the gap between the nanoplates are the smallest. Therefore, it can be concluded that with the increase of the acid pretreatment time, the LDH coatings become denser, which demonstrates that the exposure of the second phase particles promote the growth of the subsequent LDH coating. The corresponding EDS results show that the LDH coating is mainly composed of O, Mg, Al and C, and the content of Mg and O is relatively high, which suggest that the coating contains Mg-Al-LDH and $Mg(OH)_2$. As the pretreatment time of CA increases, the Al content on the surface of the subsequently prepared LDH coating increases. The content of Mg, Al and C in the CA/LDH-30s coating is higher than that of other LDH coatings, which reveals that the content of LDH in the CA/LDH-30s coating is highest. From these observations, it can be said that the CA pretreatment of 30 s has the highest influence on the growth of the subsequent LDH coatings.

Fig. 7 shows the cross-sectional morphologies and the corresponding elemental composition images of the different LDH coatings. It is apparent that the LDH coating is bonded tightly to the substrate. In addition, as the pretreatment time increases, the coating becomes denser, and the CA/LDH-30s coating is the densest without obvious cracks. The thickness of the coating is in the following order: LDH (30.82 ± 0.27 μm) < CA/LDH-10s (33.88 ± 0.42 μm) < CA/LDH-20s (37.42 ± 0.69 μm) < CA/LDH-30s (40.04 ± 0.30 μm).

3.2. Corrosion resistance

Fig. 8a shows polarization curves of AZ80, LDH, CA/LDH-10s, CA/LDH-20s and CA/LDH-30s coating. The cathodic polarization region was only used for the calculation of corrosion current density (i_{corr}). The anodic region was not considered due to the abnormal behavior (negative difference effect) exhibited by magnesium alloys during anodic dissolution [57]. To estimate i_{corr}, a slope was drawn in the cathodic branch at +100 mV from the meeting point of anodic and cathodic curves (E_{corr}) of the Tafel plot (Ref Fig. 8b). The corrosion current of the point at which the slope line intersects with the horizontal line drawn from the E_{corr} was considered as i_{corr}.

Table 2 shows the corresponding electrochemical parameters (E_{corr}, i_{corr} and β_c) of the polarization curves of the samples. The i_{corr} of the uncoated alloy is 1.25×10^{-5}A•cm^{-2}, however, with an increase of the CA treatment time, the i_{corr} constantly decreased. The i_{corr} of the CA/LDH-30s coating is about three orders of magnitude lower than that of the uncoated alloy, and one order of magnitude lower as compared with the LDH coating without acid pretreatment. Among all

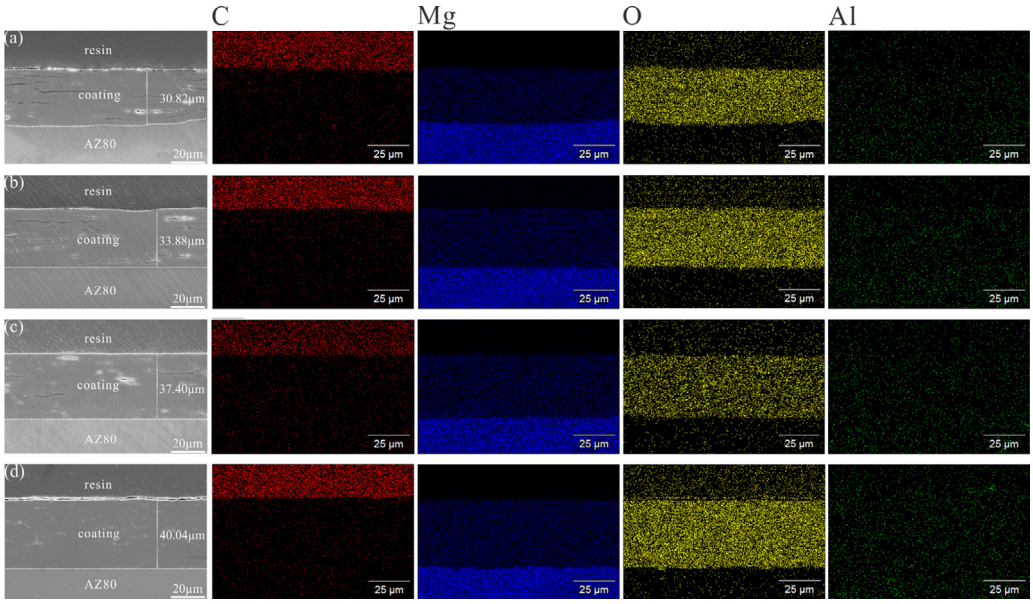

Fig. 7. Cross-sectional microstructures and corresponding elemental mapping images of (a) LDH, (b) CA/LDH-10s, (c) CA/LDH-20s and (d) CA/LDH-30s.

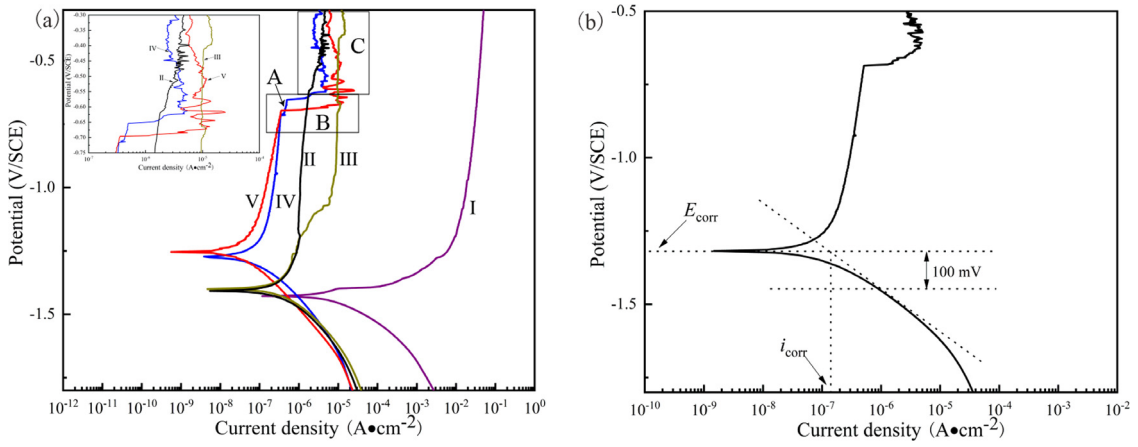

Fig. 8. (a) Polarization curves of the (I) AZ80, (II) LDH, (III) CA/LDH-10s, (IV) CA/LDH-20s and (V) CA/LDH-30s coating and (b) Illustration of determining i_{corr} from Tafel plot.

Table 2
Electrochemical parameters of the polarization curves of the samples.

Samples	E_{corr}(V/SCE)	i_{corr}(A•cm^{-2})	-β_c (mV/decade)
AZ80	−1.43	1.25 × 10^{-5}	117.70
LDH	−1.41	5.69 × 10^{-7}	179.42
CA/LDH-10 s	−1.40	5.32 × 10^{-7}	162.02
CA/LDH-20 s	−1.27	1.20 × 10^{-7}	148.03
CA/LDH-30 s	−1.25	3.85 × 10^{-8}	143.89

the coated samples, the i_{corr} of CA/LDH-30s is the lowest, indicating the best corrosion resistance.

The existence of the passive current density (point A) indicates that the coating is destroyed under the condition, where the potential is referred as the breakdown potential. Chloride ions present on the surface of the LDH coating are responsible for the breakdown of LDH coating. It is noted that a sharp increase in current density is observed with further increase in potential in the anodic direction (region B). While as the potential increases (region C), the current density has a reciprocating fluctuation process, which means the coating undergoes a repeated process of destruction and repair, suggesting a strong self-healing property due to the ion-exchangeable and diffusion behavior of the coating [58,59]. The detailed explanation about the corrosion progress will be discussed in the subsequent Section 3.4.

Fig. 9a–f shows the EIS curves of the alloy substrate and with different LDH coatings tested in 3.5 wt.% NaCl solution. As seen in Fig. 9a, the |Z| modulus of the samples at the low frequency region can be arranged in an ascending order as follows: AZ80 substrate < LDH < CA/LDH-10s < CA/LDH-20s < CA/LDH-30s coating. A higher |Z| modulus at lower frequencies indicates that the coating has better corrosion resistance. Therefore, it can be said that the CA/LDH-30s coating has the best corrosion resistance. The Bode phase angle diagrams of all the LDH coatings shown in Fig. 9b

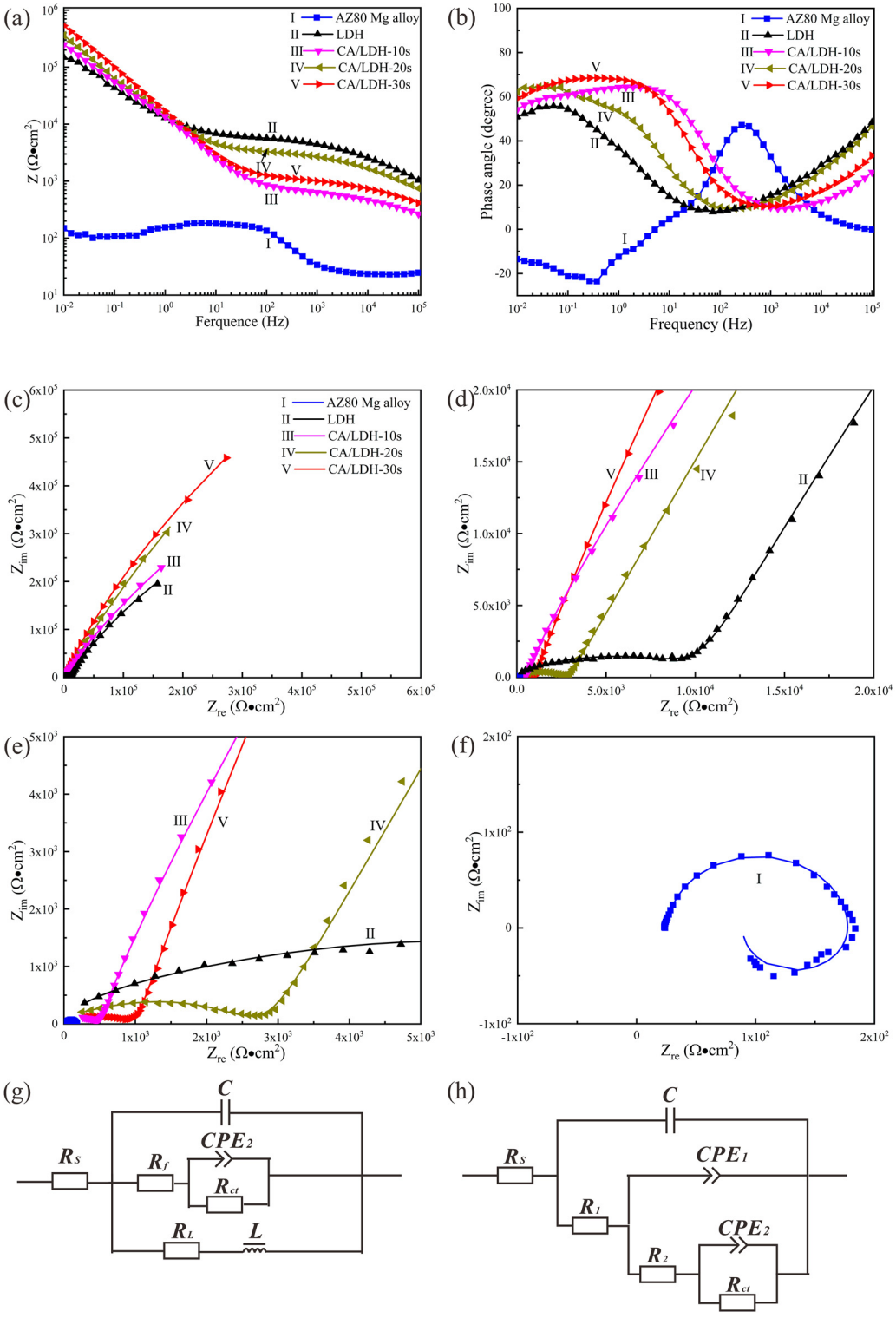

Fig. 9. EIS of (I) Mg alloy AZ80, (II) LDH, (III) CA/LDH-10s, (IV) CA/LDH-20s and (V) CA/LDH-30s: (a) Bode plots of |Z| vs. frequency, (b) Bode plots of phase angle vs. frequency, (c) Nyquist plots and (d-f) enlarged Nyquist plots; Equivalent circuits of (g) AZ80 substrate and (h) LDH coatings.

exhibit two times constants, corresponding to the loose and porous outer layer and the dense inner barrier layer of the LDH coating Fig. 9c–f reveals two capacitive loops, which could be due to the two structural layers of the LDH coating. The radius of curvature of the CA/LDH-30s coating sample is much larger than that of the other samples, indicating that the CA/LDH-30s coating has the best corrosion resistance.

Fig. 9g-h show the equivalent circuit (EC) diagrams used in this study for fitting the EIS results, and the fitted data are listed in Table 3. The EC for the uncoated alloy is shown

Table 3
Electrochemical data obtained via equivalent circuit fitting of EIS curves.

Samples	Substrate	LDH	CA/LDH-10 s	CA/LDH-20 s	CA/LDH-30 s
R_s (Ω•cm^2)	23.28	127.10	130.90	81.49	147.10
C (F•cm^{-2})	5.84 × 10^{-6}	1.09 × 10^{-9}	7.43 × 10^{-9}	1.15 × 10^{-9}	3.70 × 10^{-9}
R_f (Ω•cm^2)	2.27 × 10^1	–	–	–	–
R_1 (Ω•cm^2)	–	6.75 × 10^2	1.97 × 10^2	6.22 × 10^2	3.73 × 10^2
CPE_1 (Ω^{-1}•s^n•cm^{-2})	–	3.27 × 10^{-6}	1.27 × 10^{-5}	1.22 × 10^{-6}	3.89 × 10^{-6}
n_1	–	0.41	0.58	0.55	0.59
R_2 (Ω•cm^2)	–	1.13 × 10^4	2.53 × 10^2	2.70 × 10^3	6.78 × 10^3
CPE_2 (Ω^{-1}•s^n•cm^{-2})	6.78 × 10^{-6}	2.27 × 10^{-5}	9.78 × 10^{-6}	1.95 × 10^{-5}	1.06 × 10^{-5}
n_2	0.93	0.74	0.86	0.73	0.84
R_{ct} (Ω•cm^2)	1.85 × 10^2	2.06 × 10^6	3.35 × 10^6	4.37 × 10^6	6.17 × 10^6
R_L (Ω•cm^2)	1.37 × 10^2	–	–	–	–
L (H•cm^{-2})	1.14 × 10^2	–	–	–	–

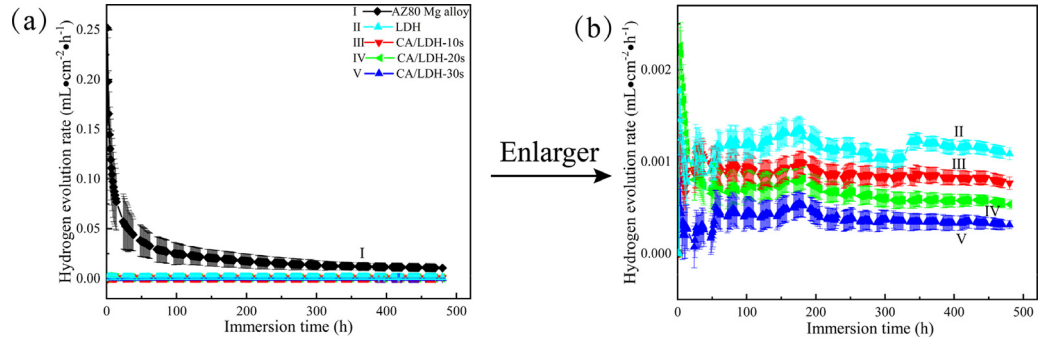

Fig. 10. (a, b) Hydrogen evolution rate (HER) plot (I) AZ80 substrate, (II) LDH, (III) CA/LDH-10s, (IV) CA/LDH-20s and (V) CA/LDH-30s in 3.5 wt.% NaCl solution for 480 h.

in Fig. 9g, where the high frequency region is composed of charge transfer resistance (R_{ct}) and interface diffusion constant phase component (CPE_2), indicating that a loose porous corrosion product film is formed on the magnesium substrate. This is mainly because the electrolyte penetrates through the corrosion product layer on the surface of the substrate. R_f is the film resistance, and C is the corresponding film capacitor. The low frequency region is composed of inductance (L) and resistance (R_L), which indicates that pitting corrosion has occurred in the alloy. The LDH coatings prepared by acid pretreatment and without acid pretreatment show similar Nyquist diagrams, which can be represented by the same equivalent circuit in Fig. 9h. The circuit elements include R_{ct}, R_f, R_1, R_2, CPE_2, as well as a porous outer capacitor (C) and a dense inner capacitor (CPE_1). R_1 and R_2, respectively represent the outer layer resistance and the inner layer resistance of the LDH coating. It is well known that the higher R_{ct} value indicates improved corrosion resistance. In Table 3, the R_{ct} value of the CA/LDH-30s coating is the highest among all the samples, indicating that it has the best corrosion resistance and can provide the best protection for the substrate.

Fig. 10 shows that the HER of the uncoated alloy is much higher than that of the LDH coated samples. When the immersion time reaches about 3 h, the HER of the alloy drops sharply, which is related to the dissolution of the substrate and the formation of $Mg(OH)_2$ precipitation. As the immersion time increases, the corrosion product deposited on the substrate which protected the substrate to a certain extent. Therefore, the HER curve of the alloy becomes relatively flat. It is worth noting that the overall HER curve of the LDH, CA/LDH-10s, CA/LDH-20s and CA/LDH-30s coatings show downward trend. The LDH coating stabilized after an immersion of 350 h, while the coating with CA pretreated tends to be stable after 190 h, which is mainly due to the protective effect of the corrosion product film formed on the surface of the coating. The HER of the CA/LDH-30s coating was the lowest throughout the test period among all coatings, which means that the coating provide the best and long-term protection.

Fig. 11 shows the SEM images of the uncoated alloy and different LDH coated alloy immersed in 3.5 wt.% NaCl for 480 h. It can be seen from Fig. 11a that the surface of alloy was severely damaged after immersion. As compared with the LDH coating before corrosion (Fig. 5a) the surface morphology of the LDH (Fig. 11b) has completely disappeared and also a few cracks appeared. For the CA/LDH-10s coating (Fig. 11c), the LDH morphology has completely changed as compared with the original sample (Fig. 5b). However, there are no obvious corrosion pits and cracks on the surface. For the CA/LDH-20 s coating, the morphology of the LDH basically remained unchanged, but corrosion pits appeared on the surface. The CA/LDH-30s coating had no corrosion cracks and corrosion pits, indicating that it has the best long-term protection for the substrate Fig. 11f shows that the ratio of

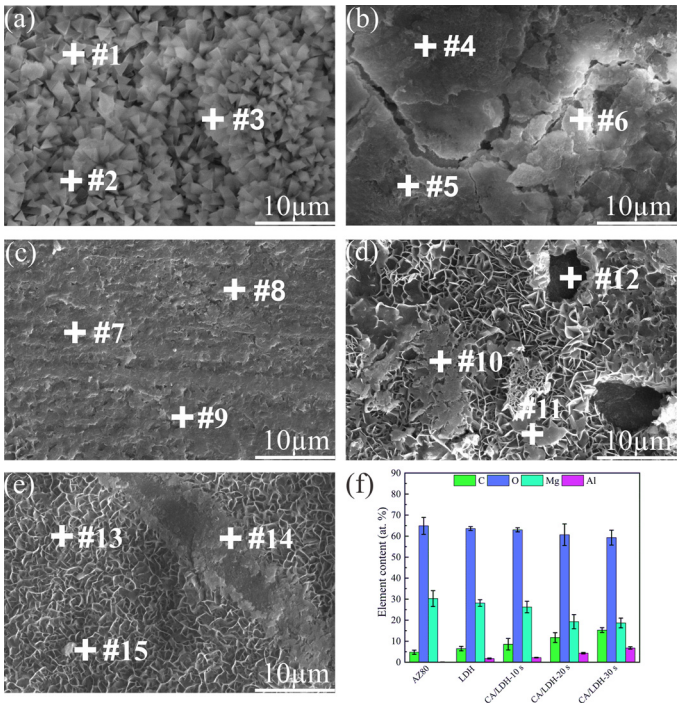

Fig. 11. SEM images of (a) AZ80 Mg alloy, (b) LDH, (c) CA/LDH-10s, (d) CA/LDH-20s and (e) CA/LDH-30s after immersion in the 3.5 wt.% NaCl solution for 480h and (f) corresponding element composition.

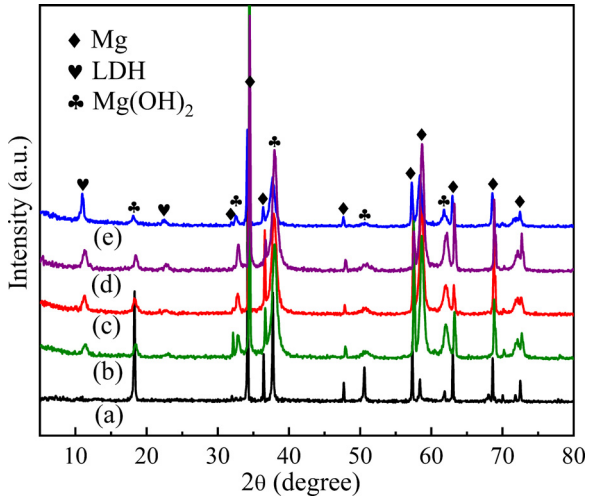

Fig. 12. XRD patterns of (a) AZ80 substrate, (b) LDH, (c) CA/LDH-10s, (d) CA/LDH-20s and (e) CA/LDH-30s after immersion in the 3.5 wt.% NaCl solution for 480h.

element O and Mg in all samples is very high, which indicates the formation of corrosion product $Mg(OH)_2$. The C and Al content of original LDH coating and CA/LDH-10s LDH coatings is the lowest, while the Mg content is the highest, which implies that severe corrosion has occurred. In addition, for the CA/LDH-20s and CA/LDH-30s coatings, the content of C and Al is higher, indicating that the corrosion is relatively low.

In order to further determine the corrosion products, XRD analysis was carried out on the coatings Fig. 12 shows the

Table 4
Elemental compositions of selected spectrum on LDH coatings as shown in Fig. 13 (at.%).

Point	Mg	O	Al	C	Mn
#1	12.44	10.48	41.96	12.64	22.47
#2	32.40	26.46	15.81	25.33	–
#3	79.58	3.17	0.48	16.68	0.09
#4	33.15	16.31	25.96	7.37	17.20
#5	12.26	11.83	25.05	36.15	14.72
#6	67.08	21.82	0.62	10.42	0.06
#7	22.52	65.32	2.22	9.94	–
#8	26.04	62.81	1.96	9.19	–
#9	28.79	59.16	1.38	10.67	–

XRD patterns of the alloy and different LDH coated alloy immersed in 3.5 wt.% NaCl solution for 480 h. All samples exhibited diffraction peaks, i.e., at 18.3°, 37.6°, 58.2° and 62.8°, indicating that the corrosion product is mainly $Mg(OH)_2$. In Fig. 12b–e, there are diffraction peaks of LDH at 11.3° and 22.6°. In Fig. 12b, the diffraction peak of LDH is the smallest, which suggests that the corrosion of LDH is more serious corresponding to the morphology in Fig. 11b, CA/LDH-30s has a strong diffraction peak, indicating that the structure of CA/LDH is stable and can provide long-term effective protection.

3.3. Formation mechanism of LDH coatings

Fig. 13 shows the SEM images of CA/LDH-0.5h, CA/LDH-1.5h and CA/LDH-3h, and the corresponding element composition is listed in Table 4. In the first stage (reaction for 0.5 h), the α-Mg phase around Al_8Mn_5 as well as $Mg_{17}Al_{12}$ in the alloy substrate begins to dissolve, forming a network of $Mg(OH)_2$ Table 4 spectra 1 and 2). The higher content of Al and Mn at the nucleation of $Mg(OH)_2$ implys that the nucleation is located near the second phase in the alloy. This is due to the higher potential of the second phase particles which act as the cathode, while the α-Mg with lower potential acts as the anode for galvanic corrosion. The specific chemical reactions are as follows ((1)–(3).

$$Mg \rightarrow Mg^{2+} + 2e^- \quad (1)$$

$$2H_2O + 2e^- \rightarrow H_2\uparrow + 2OH^- \quad (2)$$

$$Mg + 2H_2O \rightarrow Mg(OH)_2\downarrow + H_2\uparrow \quad (3)$$

In the second stage (reaction for 1.5 h), with the growth of $Mg(OH)_2$, the Al^{3+} ions in the vicinity are gradually adsorb on $Mg(OH)_2$. Part of Mg^{2+} ions of $Mg(OH)_2$ is replaced by Al^{3+} ions.The LDH like a seed germinates and grow outward around the Al_8Mn_5 phase and $Mg_{17}Al_{12}$ phase in Table 4 (spectra 4 and 5) as the center (Formula (4)–(7)) [58].

Finally, in the third stage (reaction for 3 h), the nanosheet structures of LDH coating continue to grow, accompanied by substantial Al^{3+} ions deposition. As a result, thicker and

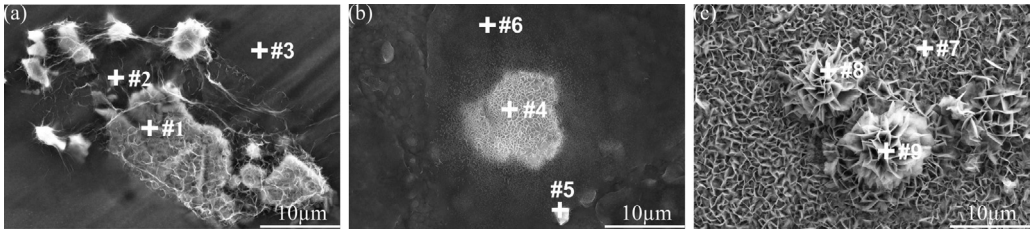

Fig. 13. SEM images of (a) CA/LDH-0.5h, (b) CA/LDH-1.5h and (c) CA/LDH-3h.

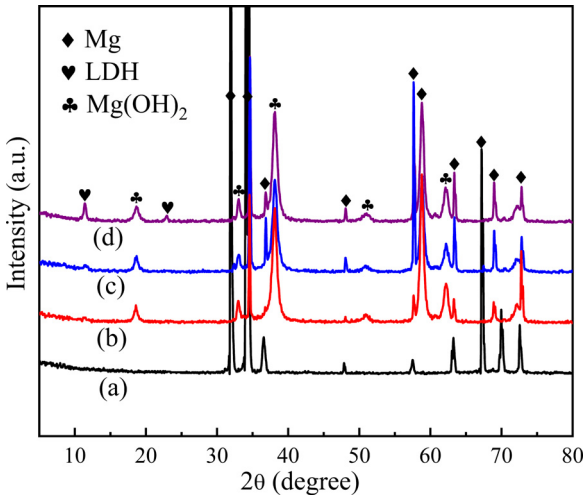

Fig. 14. XRD patterns of (a) AZ80 Mg alloy, (b) CA/LDH-0.5h, (c) CA/LDH-1.5h and (d) CA/LDH-3h.

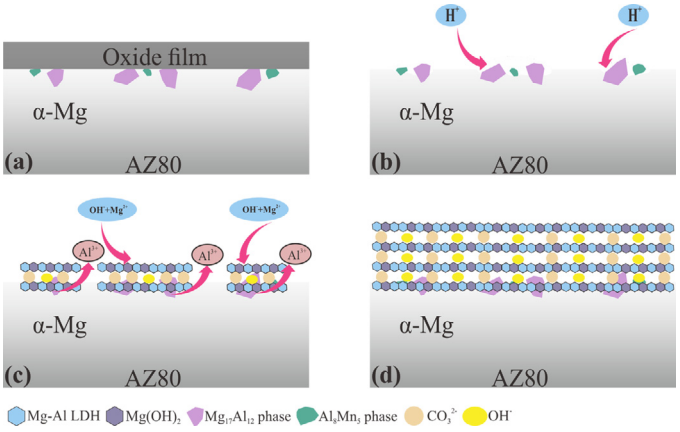

Fig. 15. Schematic diagram of formation mechanism of LDH coating on the AZ80 substrate with a prior acid pretreatment.

denser LDH coating completely cover the surface of the alloy (Table 4 spectra 7–9).

$$CO_2 + H_2O \rightarrow CO_3^{2-} + 2H^+ \quad (4)$$

$$2Mg(OH)_2 + Al^{3+} + 3OH^- \rightarrow Mg_2Al(OH)_7 \quad (5)$$

$$3Mg_2Al(OH)_7 + OH^- + 4.5H_2O \rightarrow Mg_6Al_2(OH)_{18} \cdot 4.5H_2O + Al(OH)_4^- \quad (6)$$

$$Mg_6Al_2(OH)_{18} \cdot 4.5H_2O + CO_3^{2-} \rightarrow Mg_6Al_2CO_3(OH)_{16} \cdot 4H_2O + 2OH^- + 0.5H_2O \quad (7)$$

Fig. 14 shows the XRD patterns of the (a) AZ80 Mg alloy, (b) CA/LDH-0.5h, (c) CA/LDH-1.5h and (d) CA/LDH-3h. As for the CA/LDH-0.5h sample, the peaks at about 18.4°, 37.9° and 58.6° are attributed to $Mg(OH)_2$, which suggested that sole $Mg(OH)_2$ was produced. With the increasement of reaction time (1.5 h, 3 h), the two peaks at approximately 11.3° and 22.6° appeared which are assigned to the (003) and (006) diffraction peaks of the LDH. In summary, the obtained coatings are mainly composed of $Mg(OH)_2$ and LDH Eqs. (2)–(11).

Fig. 15a–d is a schematic diagram of the growth mechanism of LDH coating on acid pretreated alloy. In summary, the formation of LDH can be divided into four stages: (a) the dissolution of the oxide layer on the surface of the alloy; (b) the dissolution of α-Mg matrix near the $Mg_{17}Al_{12}$ and Al_8Mn_5 phases; (c) the steam react with the Mg^{2+} from the alloy and the Al^{3+} from the second phase to form $Mg(OH)_2$ and LDH. CO_3^{2-} ions are provided by CO_2 in the air. Some Mg^{2+} ions in $Mg(OH)_2$ are replaced by Al^{3+} ions to form Mg-Al-CO_3^{2-}-LDH; (d) the LDH structure continuously grows and covers the surface of substrate.

Fig. 16 shows the relationship between the thickness of coating and corrosion current density as a function of second phase particles surface area fraction. The higher surface area fraction of second phase particles relates to higher thickness of the coating and lower corrosion current density. Therefore, the second phase particles have an important part in increasing the coating thickness and enhancing the anti-corrosion performance of the coating.

Fig. 17 shows the XPS full spectrums of the (a) CA/LDH-0.5h (b) CA/LDH-3h and the peak of C 1s for (c) CA/LDH-0.5h (d) CA/LDH-1.5h and (e) CA/LDH-3h. Characteristic lines of elemental magnesium, oxygen, carbon, aluminum and zinc are clearly presented. As can be seen from Fig. 17c–e, the C 1s spectra can be resolved into three peaks: main peak at 284.7 eV attributed to C-C, and two peaks at 286.1 eV and 288.5 eV that may be related to C-O and C=O group. The group of C=O and C-O reveal the presence of CA. CA has a certain complexing ability with metal ions, which can promote the reaction of Mg^{2+} and Al^{3+} during the formation of Mg-Al-LDH coating. To further explore the role of CA, C element

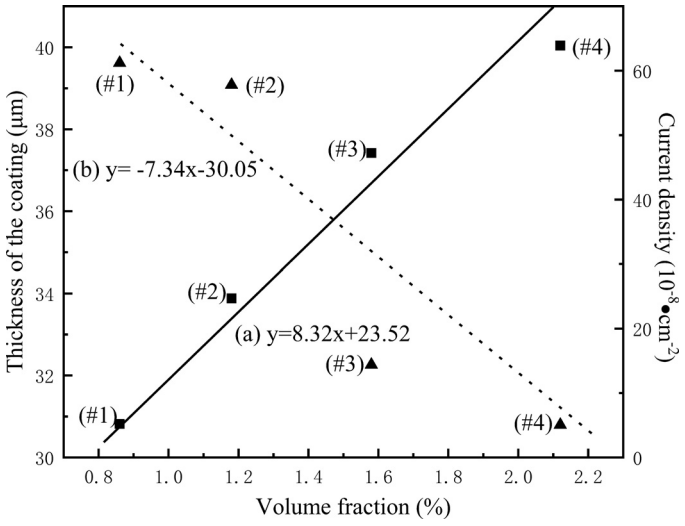

Fig. 16. Relationship between (a) thickness, (b) corrosion current density of (#1) LDH, (#2) CA/LDH-10s, (#3) CA/LDH-20s(#3) CA/LDH-30s and surface area fraction of second phase.

was detected for three different reaction periods shown in Fig. 17.

As can be observed in Fig. 17c–e, the fitted peaks at approximately 288.5 was attributed to the carboxyl [60], and at the three stages, the presence of C=O group can be detected on the surface of the sample, which may be due to a thin film produced by the reaction of CA with the AZ80 substrate in the acid process. Therefore, it can prove that CA plays a role in the formation of the coating.

3.4. Corrosion mechanism of LDH coatings

Fig. 18 shows the corrosion mechanism diagram of the LDH coating formed after the alloy pretreated with CA.The

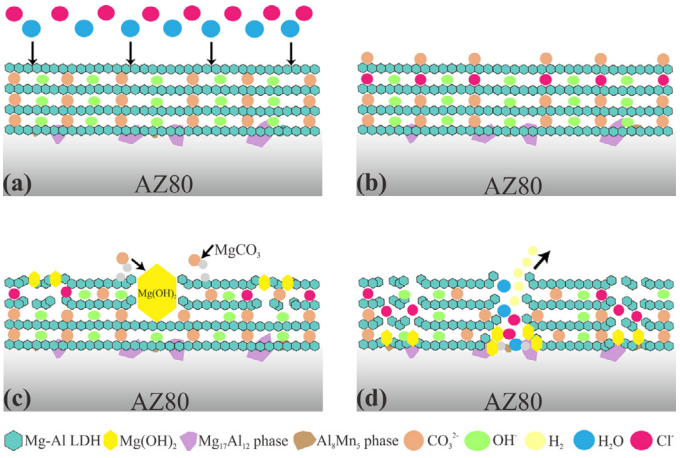

Fig. 18. Schematic diagram of corrosion mechanism of the LDH coating on the AZ80 substrate with a prior CA pretreatment.

corrosion mechanism of the coating on the alloy can be divided into three steps: (a) the LDH coating attracts corrosive Cl^- through ion exchange reaction Fig. 18b); (b) the coating is destroyed in the vicinity of $Mg_{17}Al_{12}$ and Al_8Mn_5 phase and form corrosion products, and the accumulated corrosion products form a secondary protection (Fig. 18c); (c) the corrosive media reacts with the substrate to produce a large amount of corrosion products and hydrogen gas, causing the coating to rupture (Fig. 18d). The specific reactions follow as ((8)–(12)

$$LDH - CO_3^{2-} + Cl^- \rightarrow LDH - Cl^- + CO_3^{2-} \quad (8)$$

$$Mg^{2+} + CO_3^{2-} \rightarrow MgCO_3 \downarrow \quad (9)$$

$$MgCO_3 + 2OH^- \rightarrow Mg(OH)_2 \downarrow + CO_3^{2-} \quad (10)$$

$$Mg(OH)_2 + 2Cl^- \rightarrow MgCl_2 + 2OH^- \quad (11)$$

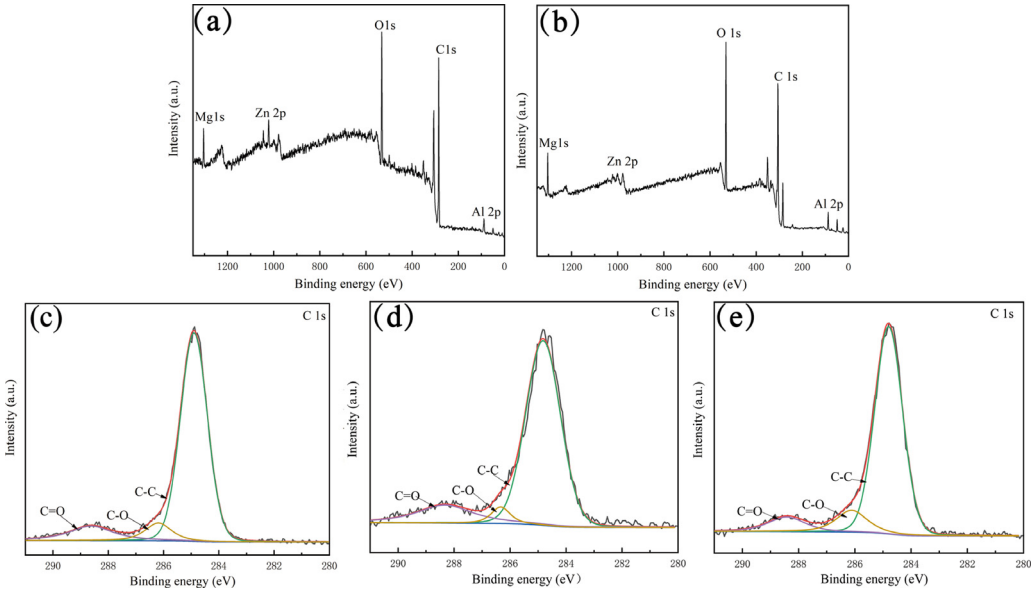

Fig. 17. XPS full spectrums of the (a) CA/LDH-0.5h (b) CA/LDH-3h and the peak of C 1s for (c) CA/LDH-0.5h (d) CA/LDH-1.5h and (e) CA/LDH-3h.

$$Mg + 2H_2O \rightarrow Mg(OH)_2 \downarrow + H_2 \uparrow \quad (12)$$

4. Conclusions

Based on the experimental results and analysis, the following conclusion are made:

(1) A signficant amount of $Mg_{17}Al_{12}$ and Al_8Mn_5 particles are exposed on the surface of AZ80 magnesium alloy after the CA pretreatment. As the pretreatment time increased, the surface area fraction of the second phase particles on the surface of the alloy also increased. As compared with the polished alloy, the surface area fraction of the second phase particles on CA/AZ80-30s, CA/AZ80-20s and CA/AZ80-10s increased by 3 times, 2 times and 1.5 times, respectively. As a result, the surface roughness of the alloy increased about 3 times.

(2) The i_{corr} of the LDH coating after CA pretreatment is lower than that of the coating without acid pretreatment (i_{corr} is 5.69×10^{-7} A•cm^{-2}). The decrease in the i_{corr} of the CA/LDH-10 s coated alloy is only marginal as compared to the other coatings. The i_{corr} of the CA/LDH-20 s coated alloy is 4 times lower than that of the LDH coated alloy without acid pretreatment, and the i_{corr} of the CA/LDH-30 s coated alloy (i_{corr} is 3.85×10^{-8} A•cm^{-2}) is one order of magnitude lower than that of the LDH coated alloy without acid pretreatment. The results indicates that CA pretreatment can effectively improve the corrosion protection performance of the LDH coating.

(3) CA pretreatment increases the exposoure of $Mg_{17}Al_{12}$ and Al_8Mn_5 particles on the AZ80 Mg alloy. While the α-Mg phase (anode) corrodes, the $Mg_{17}Al_{12}$ and Al_8Mn_5 particles, being cathode, are unaffected and thereby increases the Al content on the surface of the alloy. The exposure of $Mg_{17}Al_{12}$ and Al_8Mn_5 particles plays important role in the growth of LDH coatings and thereby increases the corrosion protection performance of the coatings.

Declaration of Competing Interest

The authors declare that they have no known competing financial interests or personal relationships that could have appeared to influence the work reported in this paper.

Acknowledgments

This work was supported by the National Natural Science Foundation of China (Grant Nos. 51601108 and 52071191) and the Natural Science Foundation of Shandong Province (ZR2020ME011).

References

[1] L.Y. Cui, L. Gao, J.C. Zhang, Z. Tang, X.L. Fan, J.C. Liu, D.C. Chen, R.C. Zeng, S.Q. Li, K.Q. Zhi, J. Magnes. Alloy. 9 (2021) 266–280.
[2] X.L. Fan, Y.F. Huo, C.Y. Li, M.B. Kannan, X.B. Chen, S.K. Guan, R.C. Zeng, Q.L. Ma, Rare Met. 38 (2019) 520–531.
[3] C. Zhao, F. Cao, G.L. Song, J. Magnes. Alloy. 8 (2020) 150–162.
[4] Y. Song, Y. Tang, L. Fang, F. Wu, X. Zeng, J. Hu, S.F. Zhang, B. Jiang, H. Luo, J. Magnes. Alloy. 9 (2021) 658–667.
[5] Z.Z. Yin, W.C. Qi, R.C. Zeng, X.B. Chen, C.D. Gu, S.K. Guan, Y.F. Zheng, J. Magnes. Alloy. 8 (2020) 42–65.
[6] T.T.T. Trang, J.H. Zhang, J.H. Kim, A. Zargaran, J.H. Hwang, B.C. Suh, N.J. Kim, Nat. Commun. 9 (2018) 2522.
[7] Z.Y. Ding, L.Y. Cui, X.B. Chen, R.C. Zeng, S.K. Guan, S.Q. Li, F. Zhang, Y.H. Zou, Q.Y. Liu, J. Alloy. Compd. 764 (2018) 250–260.
[8] Y.G. Li, Y.H. Wei, L.F. Hou, P.J. Han, Corros. Sci. 69 (2013) 67–76.
[9] J. Chen, Y. Song, D. Shan, E.H. Han, Corros. Sci. 65 (2012) 268–277.
[10] R.C. Zeng, F. Zhang, Z.D. Lan, H.Z. Cui, E.H. Han, Corros. Sci. 88 (2014) 452–459.
[11] J. Wang, L.Y. Cui, Y.D. Ren, Y.H. Zou, J.L. Ma, C.J. Wang, Z.Y. Zheng, X.B. Chen, R.C. Zeng, Y.F. Zheng, J. Mater. Sci. Technol. 47 (2020) 52–67.
[12] Y.H. Zou, J. Wang, L.Y. Cui, R.C. Zeng, Q.Z. Wang, Q.X. Han, J. Qiu, X.B. Chen, D.C. Chen, S.K. Guan, Y.F. Zheng, Acta Biomater. 98 (2019) 196–214.
[13] C.Y. Zhang, R.C. Zeng, C.L. Liu, J.C. G, Surf. Coat. Tech. 204 (2010) 3636–3640.
[14] R.C. Zeng, E.H. Han, W. Ke, Int. J. Fatigue 36 (2012) 40–46.
[15] D. Zhang, F. Peng, X.Y. Liu, J. Magnes. Alloy. 853 (2021) 157010.
[16] J.H. Dou, H.J. Yu, Chen C.Z, R. Lok-Wang Ma, M. Ming-Fai Yuen, Mater. Lett. 271 (2020) 127729.
[17] L.Y. Cui, R.C. Zeng, S.K. Guan, W.C. Qi, F. Zhang, S.Q. Li, E.H. Han, J. Alloy. Compd. 695 (2017) 2464–2476.
[18] J.Z. Lin, W.D. Chen, Q.Q. Tang, L.Y. Cao, S.H. Su, Surf. Interfaces 22 (2021) 100805.
[19] L.Y. Li, L.Y. Cui, B. Liu, R.C. Zeng, X.B. Chen, S.Q. Li, Z.L. Wang, E.H. Han, Appl. Surf. Sci. 465 (2019) 1066–1077.
[20] L. Wu, X. Ding, Z. Zheng, Y. Ma, A. Atrens, X. Chen, Z. Xie, D. Sun, F. Pan, Appl. Surf. Sci. 487 (2019) 558–568.
[21] J. Jayaraj, K.R. Rajesh, S. Amruth Raj, A. Srinivasan, S. Ananthakumar, N.G.K. Dhaipule, S.K. Kalpathy, U.T.S. Pillai, U.K. Mudali, J. Alloy. Compd. 784 (2019) 1162–1174.
[22] L.Y. Cui, J. Xu, N. Lu, R.C. Zeng, Y.H. Zou, S.Q. Li, F. Zhang, T. Nonferr, Met. Soc. 27 (2017) 1081–1086.
[23] L.Y. Cui, R.C. Zeng, X.X. Zhu, T.T. Pang, S.Q. Li, F. Zhang, Front. Mater. Sci. 10 (2016) 134–146.
[24] Y. Zhao, Z. Zhang, L. Shi, F. Zhang, S. Li, R. Zeng, Mater. Lett. 237 (2019) 14–18.
[25] C.A. Chen, S.Y. Jian, C.H. Lu, C.Y. Lee, S.L. Aktuğ, M.D. Ger, J. Mater. Res. Technol. 9 (2020) 13902–13913.
[26] J. Jin, C. Liu, S. Fu, Y. Gao, X. Shu, Surf. Coat. Tech. 206 (2011) 348–353.
[27] Z. Liu, W. Gao, Surf. Coat. Tech. 200 (2006) 3553–3560.
[28] Z.M. Qiu, R.C. Zeng, F. Zhang, L. Song, S.Q. Li, T. Nonferr. Met. Soc. 30 (2020) 2967–2979.
[29] K. Cao, Z. Yu, L. Zhu, D. Yin, L. Chen, Y. Jiang, J. Wang, Surf. Coat. Tech. 407 (2021) 126763.
[30] J.K.E. Tan, P. Balan, N. Birbilis, Appl. Clay. Sci. 202 (2021) 105948.
[31] Z.H. Wang, J.M. Zhang, Y. Li, L.J. Bai, G.J. Zhang, Trans. Nonferr. Met. Soc. 29 (2019) 2066–2077.
[32] J. Chen, J. Feng, L. Yan, H. Li, C. Xiong, S. Ma, J. Magnes. Alloy. 9 (2021) 1019–1027.
[33] J. Chen, T. Jiang, X. Lan, K. Kang, F. Cai, S. Ma, Mater. Today Phys. 20 (2021) 100474.
[34] T. Hu, Y. Ouyang, Z.H. Xie, L. Wu, J. Mater. Sci. Technol. 92 (2021) 225–235.
[35] C. Li, J. Chen, Y. Wu, W. Cao, S. Sang, Q. Wu, H. Liu, K. Liu, Int. J. Hydrog. Energy 44 (2019) 2656–2663.
[36] Y.L. Wu, L. Wu, W.H. Yao, B. Jiang, J.H. Wu, Y.N. Chen, X.B. Chen, Q. Zhan, G. Zhang, F.S. Pan, Electrochim. Acta 374 (2021) 137913.

[37] Y.L. Wu, L. Wu, M.L. Zheludkevich, Y.N. Chen, M.L. Serdechnova, W. Yao, C. Blawert, A. Atrens, F.S. Pan, J. Mater. Sci. Technol. 91 (2021) 28–39.
[38] F. Zhang, Z.G. Liu, R.C. Zeng, S.Q. Li, H.Z. Cui, L. Song, E.H. Han, Surf. Coat. Tech. 258 (2014) 1152–1158.
[39] A. Khataee, T. Sadeghi Rad, S. Nikzat, A. Hassani, M.H. Aslan, M. Kobya, E. Demirbaş, Chem. Eng. J. 375 (2019) 122102.
[40] Y.X. Zhu, G.L. Song, P.P. Wu, J.F. Huang, D.J. Zheng, J. Alloy. Compd. 855 (2021) 157550.
[41] D. Jiang, X. Xia, J. Hou, G. Cai, X. Zhang, Z. Dong, Chem. Eng. J. 373 (2019) 285–297.
[42] V. Melchor-Lagar, E. Ramos-Ramírez, A.A. Morales-Pérez, I. Rangel-Vázquez, G. Del Angel, J. Photochem. Photobiol. A 389 (2020) 112251.
[43] T. Stimpfling, F. Leroux, H. Hintze-Bruening, Appl. Clay. Sci. 83–84 (2013) 32–41.
[44] T. Ishizaki, S. Chiba, H. Suzuki, ECS Electrochem. Lett. 2 (2013) C15–C17.
[45] T. Ishizaki, S. Chiba, K. Watanabe, H. Suzuki, J. Mater. Chem. A 1 (2013) 8968–8977.
[46] N. Kamiyama, G. Panomsuwan, E. Yamamoto, T. Sudare, N. Saito, T. Ishizaki, Surf. Coat. Tech. 286 (2016) 172–177.
[47] G.J. Gao, M.Q. Zeng, E.L. Zhang, R.C. Zeng, L.Y. Cui, D.K. Xu, F.Q. Wang, M.B. Kannan, J. Mater. Sci. Technol. 83 (2021) 161–178.
[48] J.Y. Zhang, B. Jiang, Q.S. Yang, D. Huang, A. Tang, F.S. Pan, Q.Y. Han, J. Alloy. Compd. 849 (2020) 156619.
[49] Y.H. Huang, Y.L. Lee, C.S. Lin, J. Electrochem. Soc. 158 (158) (2011) C310.
[50] H.H. Elsentriecy, K. Azumi, H. Konno, Surf. Coat. Tech. 202 (2007) 532–537.
[51] V.M. Azevedo, M.V. Dias, H.H. de Siqueira Elias, K.L. Fukushima, E.K. Silva, J. de Deus Souza Carneiro, N. de Fatima Ferreira Soares, S.V. Borges, Food Res. Int. 107 (2018) 306–313.
[52] Z.Y. Ding, L.Y. Cui, R.C. Zeng, Y.B. Zhao, S.K. Guan, D.K. Xu, C.G. Lin, J. Mater. Sci. Technol. 34 (2018) 1550–1557.
[53] C.Y. Li, X.L. Feng, X.L. Fan, X.T. Yu, Z.Z. Yin, M.B. Kannan, X.B. Chen, S.K. Guan, J. Zhang, R.C. Zeng, Adv. Eng. Mater. 21 (2019) 1900446.
[54] Y.B. Zhao, X.Y. Chen, S.Q. Li, R.C. Zeng, F. Zhang, Z.L. Wang, S.K. Guan, J. Colloid Interface Sci. 547 (2019) 309–317.
[55] F. Andreatta, I. Apachitei, A.A. Kodentsov, J. Dzwonczyk, J. Duszczyk, Electrochim. Acta 51 (2006) 3551–3557.
[56] X. Jia, J. Song, B. Xiao, Q. Liu, H. Zhao, Z. Yang, J. Liao, L. Wu, B. Jiang, A. Atrens, F.S. Pan, J. Mater. Res. Technol. 14 (2021) 1739–1753.
[57] J. Jayaraj, S. Amruth Raj, A. Srinivasan, S. Ananthakumar, U.T.S. Pillai, N.G.K. Dhaipule, U.K. Mudali, Corros. Sci. 113 (2016) 104–115.
[58] C.Y. Li, L. Gao, X.L. Fan, R.C. Zeng, D.C. Chen, K.Q. Zhi, Bioact. Mater. 5 (2020) 364–376.
[59] M. Kaseem, Y.G. Ko, Ultrason. Sonochem. 49 (2018) 316–324.
[60] K.Y. Cao, Z.X. Yu, L.J. Zhu, D. Yin, L.G. Chen, Y. Jiang, J. Wang, Surf. Coat. Tech. 407 (2021) 126763.